JOURNAL OF SYNCHROTRON RADIATION
ISSN 1600-5775

In situ synchrotron X-ray diffraction investigation of the evolution of a $PbO_2/PbSO_4$ surface layer on a copper electrowinning Pb anode in a novel electrochemical flow cell. Corrigendum

Marie Clancy,[a]* Mark J. Styles,[b] Colleen J. Bettles,[a] Nick Birbilis,[a] Miao Chen,[c] Yansheng Zhang,[c] Qinfen Gu,[d] Justin A. Kimpton[d] and Nathan A. S. Webster[c]*

[a]ARC Centre of Excellence for Design in Light Metals, Department of Materials Engineering, Monash University, Clayton, VIC 3800, Australia, [b]CSIRO Manufacturing Flagship, Bayview Avenue, Clayton, VIC 3168, Australia, [c]CSIRO Mineral Resources Flagship, Private Bag 10, Clayton South, VIC 3169, Australia, and [d]Australian Synchrotron, 800 Blackburn Road, Clayton, VIC 3168, Australia. *Correspondence e-mail: marie.clancy@monash.edu, nathan.webster@csiro.au

Received 16 April 2015
Accepted 16 April 2015

Keywords: PbO_2; $PbSO_4$; electrochemical cycling; flow cell; *in situ* X-ray diffraction; Rietveld refinement; quantitative phase analysis.

Figures 7 and 8 of the article by Clancy *et al.* [(2015), *J. Synchrotron Rad.* **22**, 366–375] are corrected.

In the article by Clancy *et al.* (2015), Fig. 8(*a*), showing the results of quantitative phase analysis, was incorrect. The values shown in the published manuscript were determined using a preliminary and incorrect model in the Rietveld

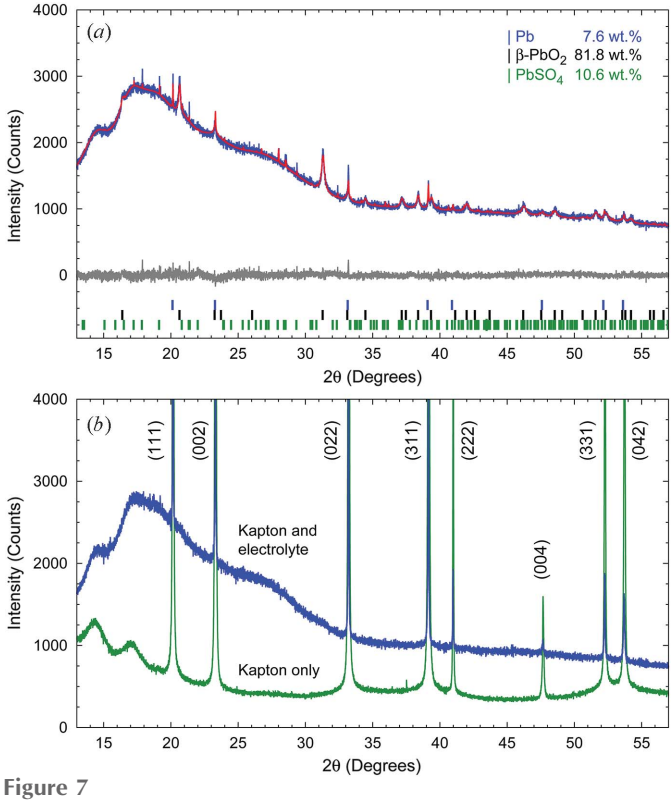

Figure 7
(*a*) Rietveld refinement output of a dataset collected during the early stages of the OCP segment of the fifth cycle (t = 320 min, R_{wp} = 2.56). The experimental data are shown as a blue solid line, the calculated pattern the red solid line, and the difference pattern the grey solid line below. The tick marks below the difference curve are the Bragg reflection markers for Pb (upper), β-PbO_2 (middle) and $PbSO_4$ (lower). (*b*) Overlay of datasets collected at the beginning of the first GALV segment (upper), and for the substrate and Kapton® film before the flow of electrolyte commenced (lower). The Pb reflections are labelled with their Miller indices.

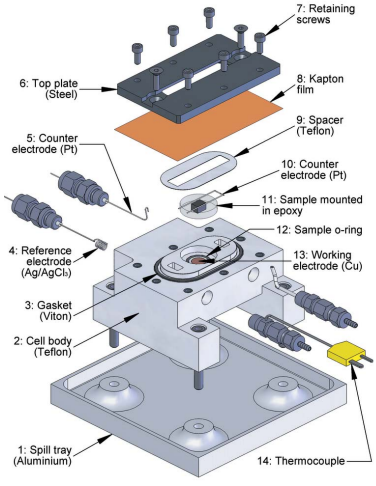

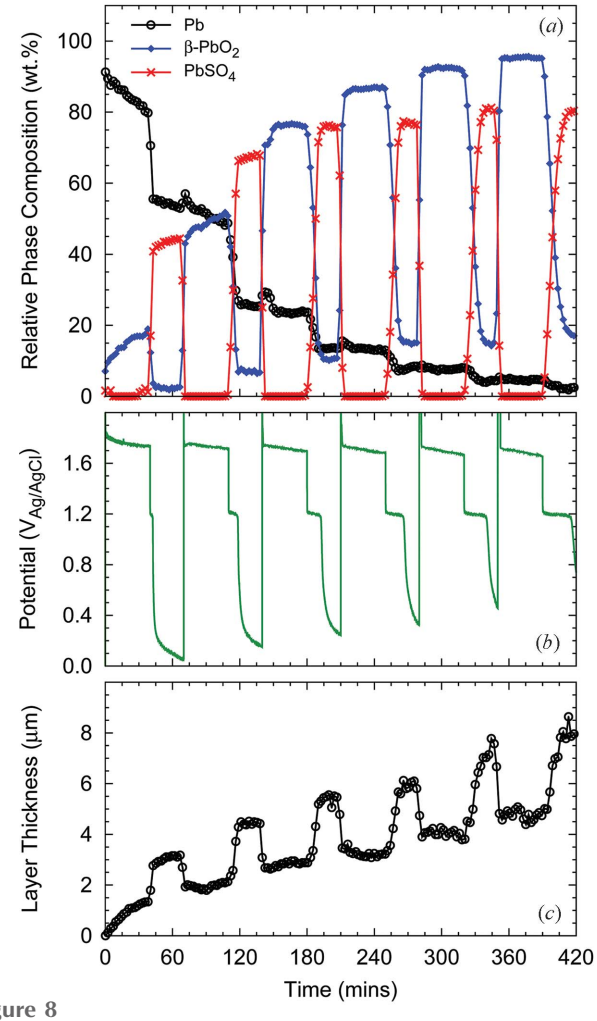

Figure 8
(*a*) Results of Rietveld refinement-based quantitative phase analysis, showing the evolution in relative concentration of the Pb substrate and the PbO_2 and $PbSO_4$ surface layers during the electrochemical test. (*b*) Potential *versus* time plot. (*c*) Estimated $PbO_2/PbSO_4$ surface layer thickness as a function of time.

refinements. The correct Fig. 8, determined using the correct model, is shown here. Due to this error, the phase concentration values quoted in Fig. 7(*a*) are incorrect; the correct Fig. 7 is also shown here.

Owing to error in Fig. 8(*a*) there are two values which are incorrect in the text immediately below the figure on page 373 of the original article. The first sentence below the figure should read 'PbO_2 formed immediately on the substrate, and continued to grow during the GALV segment of the first cycle, as indicated by the increase in crystalline phase concentration from 7 wt% at t = 0 min to 19 wt% at the end of the segment (t = 38 min).' In addition, the second sentence of the third paragraph on page 374 should read 'Since PbO_2 was present on the surface of the anode at t = 0 min [the concentration of PbO_2 in Fig. 8(*a*) is 7 wt%], the I_0 value used here in equation (6) is not the true I_0 value for a layer-free surface, which adds to the semi-quantitative nature of this approach.'

The errors occurred during the manuscript revision process, and correction of these errors does not change the outcomes or interpretations of the article.

References

Clancy, M., Styles, M. J., Bettles, C. J., Birbilis, N., Chen, M., Zhang, Y., Gu, Q., Kimpton, J. A. & Webster, N. A. S. (2015). *J. Synchrotron Rad.* **22**, 366–375.

Journal of
Synchrotron
Radiation

ISSN 1600-5775

Received 29 July 2014
Accepted 18 December 2014

In situ synchrotron X-ray diffraction investigation of the evolution of a $PbO_2/PbSO_4$ surface layer on a copper electrowinning Pb anode in a novel electrochemical flow cell

Marie Clancy,[a]* Mark J. Styles,[b] Colleen J. Bettles,[a] Nick Birbilis,[a] Miao Chen,[c] Yansheng Zhang,[c] Qinfen Gu,[d] Justin A. Kimpton[d] and Nathan A. S. Webster[c]*

[a]ARC Centre of Excellence for Design in Light Metals, Department of Materials Engineering, Monash University, Clayton, VIC 3800, Australia, [b]CSIRO Manufacturing Flagship, Bayview Avenue, Clayton, VIC 3168, Australia, [c]CSIRO Mineral Resources Flagship, Private Bag 10, Clayton South, VIC 3169, Australia, and [d]Australian Synchrotron, 800 Blackburn Road, Clayton, VIC 3168, Australia. *E-mail: marie.clancy@monash.edu, nathan.webster@csiro.au

This paper describes the quantitative measurement, by *in situ* synchrotron X-ray diffraction (S-XRD) and subsequent Rietveld-based quantitative phase analysis and thickness calculations, of the evolution of the PbO_2 and $PbSO_4$ surface layers formed on a pure lead anode under simulated copper electrowinning conditions in a 1.6 *M* H_2SO_4 electrolyte at 318 K. This is the first report of a truly *in situ* S-XRD study of the surface layer evolution on a Pb substrate under cycles of galvanostatic and power interruption conditions, of key interest to the mining, solvent extraction and lead acid battery communities. The design of a novel reflection geometry electrochemical flow cell is also described. The *in situ* S-XRD results show that β-PbO_2 forms immediately on the anode under galvanostatic conditions, and undergoes continued growth until power interruption where it transforms to $PbSO_4$. The kinetics of the β-PbO_2 to $PbSO_4$ conversion decrease as the number of cycles increases, whilst the amount of residual PbO_2 increases with the number of cycles due to incomplete conversion to $PbSO_4$. Conversely, complete transformation of $PbSO_4$ to β-PbO_2 was observed in each cycle. The results of layer thickness calculations demonstrate a significant volume change upon $PbSO_4$ to β-PbO_2 transformation.

Keywords: PbO_2; $PbSO_4$; electrochemical cycling; flow cell; *in situ* X-ray diffraction; Rietveld refinement; quantitative phase analysis.

1. Introduction

In an industrial electrowinning 'tank-house', as relevant to the production of copper (Cu) as one example, lead (Pb)-based alloy anodes are placed in a concentrated acid bath and alternated with stainless steel cathodes (Schlesinger *et al.*, 2011). Under galvanostatic conditions the Cu dissolved in the acid electrolyte is plated onto the cathode. To harvest a sheet of Cu takes about seven days, but the Pb anodes are expected to have an average lifetime of about five years (Camurri *et al.*, 2001). Electrowinning takes place under the application of a constant current, where the Pb^{2+} ions at the anode surface react with the sulfate ions in the H_2SO_4 electrolyte to produce a layer of $PbSO_4$ [equation (1), where NHE = normal hydrogen electrode] (anglesite, space group *Pnma*) (Miyake *et al.*, 1978), which may be subsequently reduced to produce a PbO_2 compound [equation (2)]. The reactions of Pb in the presence of sulfate ions are shown in Fig. 1, a Pourbaix diagram adapted for Pb in H_2SO_4 (Maksymiuk *et al.*, 2009).

$$Pb + SO_4^{2-} - 2e \rightarrow PbSO_4 \qquad -0.356\,V_{NHE}, \qquad (1)$$

$$PbSO_4 + 2H_2O - 2e \rightarrow PbO_2 + H_2SO_4 + 2H^+ \quad +1.685\,V_{NHE}. \qquad (2)$$

There are two main polymorphs of PbO_2 at ambient temperature and pressure: the orthorhombic α phase (scrutinyite, space group *Pbcn*) (Taggart *et al.*, 1988) and the tetragonal β phase (plattnerite, space group $P4_2/mnm$) (D'Antonio & Santoro, 1980). While both phases have been observed on the surface of Pb-based anodes (*e.g.* Bagshaw *et al.*, 1966; Hill, 1982), α-PbO_2 is metastable with respect to β-PbO_2 under

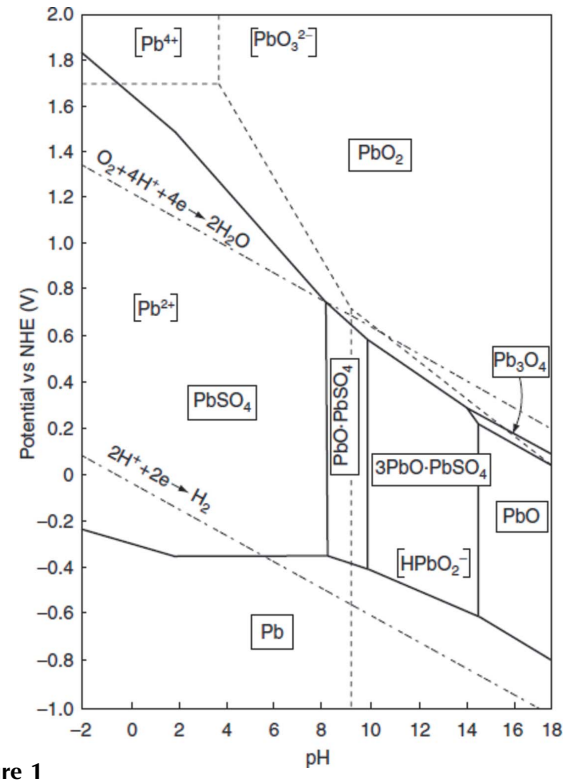

Figure 1
Pourbaix diagram for Pb in the presence of sulfate ions, at 298 K [reprinted from Maksymiuk *et al.* (2009) with permission from Elsevier]. [Republished with permission of Taylor & Francis Group LLC Books, from Sharpe, T. F. (1973). *Encyclopedia of Electrochemistry of the Elements*, Vol. 1, ch. I-5, edited by A. J. Bard, pp. 235–347. New York: Marcel Dekker; permission conveyed through Copyright Clearance Center, Inc.]

ambient conditions (White *et al.*, 1961; White & Roy, 1964) and it is the β-PbO_2 phase that forms more commonly. It is believed that different pH conditions will control the mechanism by which the PbO_2 crystals are formed (Fletcher & Matthews, 1981), and subsequently which structure forms. Ivanov *et al.* (2000) stated that α-PbO_2 forms by a reaction between a Pb complex and OH^- while β-PbO_2 results from a reaction involving a SO_4^{2-}-containing complex. Hence, α-PbO_2 forms in alkaline or neutral electrolyte while β-PbO_2 forms in acidic electrolytes. In electrowinning applications, a PbO_2 surface layer is more desirable than $PbSO_4$, as PbO_2 is often present as a dense, compact and (electron) conductive film (Pavlov, 2011), properties which are all critical to the efficiency of the Cu electrowinning process.

While research has been conducted on improving the system efficiency by altering the anode composition (Clancy *et al.*, 2013), focus is needed on the role played by the operating conditions in the tank-house. A power interruption in the cell can be compared with the charge/discharge situation in a lead acid battery (Pavlov & Monahov, 1996). The Pb anodes remain in the acid bath with no applied potential, thus permitting the PbO_2 layer to likely revert to $PbSO_4$. The length of time that it takes for the back-up power supply to be activated can have a significant effect on the subsequent performance of the surface of the Pb anode, and other research has been conducted on how to minimize the impact of such power interruptions (Nikoloski *et al.*, 2010).

During a recent laboratory-based electrochemical testing program designed to examine the durability of some novel Pb alloys, different electrochemical responses to power loss/interruption were observed. The fact that the alloys had different responses, coupled with the fact that power interruptions are guaranteed in service, highlights the need for a comprehensive understanding of the reasons behind the responses (*i.e.* what is the effect of different alloying elements on the formation/decomposition of the surface layers?). Other key questions include whether the surface becomes a homogeneous layer, for example, or if the surface is actually a multiphase system. X-ray diffraction (XRD) is the ideal technique to answer these questions as far as the crystalline phase content is concerned; it is recognized, however, that electrochemically cycled PbO_2/$PbSO_4$ has previously been shown to also contain amorphous material (Monahov & Pavlov, 1993; Pavlov & Monahov, 1996).

An *ex situ* XRD approach to surface layer characterization is inferior to an *in situ* approach, since the nature of the surface will change on extraction from the cell. In addition, using the *in situ* approach avoids artefacts induced by cell shutdown while allowing for the monitoring of any intermediate or metastable phases that may not be observable by *ex situ* techniques. There are works in the literature describing results of such *ex situ* experiments in the context of Pb anodes (Burbank, 1971; Xia & Zhou, 1995; Caballero *et al.*, 2004; Pavlov *et al.*, 2004). There are also papers describing results of *in situ* XRD studies for lead acid battery application (Herron *et al.*, 1992*a*,*b*; Nauer, 1996; Angerer *et al.*, 2009). Herron *et al.* (1992*b*) used an inert Pt anode, onto which the PbO_2 was deposited from an aqueous 0.1 *M* $Pb(NO_3)_2$ solution. The PbO_2-coated Pt anode was then placed in 1 *M* H_2SO_4 at 293 K in an electrochemical cell and held at a number of critical potentials to study the $PbSO_4$–PbO_2 transformation. The XRD patterns were, however, only collected when the potential had been stepped to the desired potentials for studying the transformation; so in fact the XRD pattern may not be a complete representation of what is happening during the transformation. This anomaly, coupled with the anode, electrolyte molarity and temperature, and the electrochemical program design, show a distinct need for the study presented in this current work.

In another related study, Nauer (1996) conducted grazing-incidence X-ray diffraction (GIXD) with Pb electrodes in 5 *M* H_2SO_4 at room temperature. The electrode was oxidized with current densities ranging from 50 to 200 A m^{-2}, and again the diffraction data were only collected at specific potentials and not throughout the entire period of electrochemical exposure. Angerer *et al.* (2009) conducted an *in situ* GIXD study of the electrochemical reactions on Pb electrodes in 1 *M* H_2SO_4 at room temperature. As with Herron, the system was switched from galvanostatic to potentiodynamic cycling and, once a critical time had been reached, only then were the diffraction data collected. Each of these studies was not truly *in situ* because data were not acquired continuously throughout

electrochemical cycling. Rather, they were only acquired under either completely charged and/or discharged conditions, with the thickness of the electrolyte layer deflated because of excessive attenuation in and scatter from the electrolyte precluding data collection throughout. Additionally, such studies were conducted in the context and conditions of Pb acid battery applications and not electrowinning, such that the electrolyte and current density specifics were also dissimilar to those presented here. The issue of true *in situ* performance is, however, critical for the industrially common and expensive process of electrowinning, where significant cost benefits can be achieved with greater anode performance. The outcomes of a truly *in situ* XRD investigation of surface layer formation on Pb-based alloys under repeated galvanostatic (operational) and OCP (power interruption) conditions are thus of key interest to the mining, solvent extraction and metal production industries, whilst also broadly relevant to the lead acid battery community.

The present work describes outcomes of a synchrotron-based *in situ* experiment, which utilizes synchrotron XRD (S-XRD) experimentation and a novel electrochemical flow cell (EFC) to allow for continuous collection of *in situ* XRD data on a pure Pb substrate under electrochemical control. Whilst there a number of electrochemical cells described in the literature employing reflection (Barlow *et al.*, 1989; Herron *et al.*, 1992*a*; Nauer, 1996; De Marco *et al.*, 2003) and transmission (Robinson & O'Grady, 1993; Nagy *et al.*, 1994; Scherb *et al.*, 1998; Rayment *et al.*, 2008; Ingham *et al.*, 2010; Ko *et al.*, 2012) geometries [a relatively recent review was provided by De Marco & Veder (2010)], this is the first such reflection-geometry (in the context of this manuscript, reflection geometry is not limited to the situation where the angle of incidence is below the critical angle for the substrate material) electrochemical cell designed specifically for uninterrupted solution flow experiments on the powder diffraction beamline at the Australian Synchrotron (Wallwork *et al.*, 2007).

2. Experimental

2.1. Cell Design

The design of the EFC is shown schematically in Fig. 2, and was based on a previous cell described by Webster *et al.* (2009). The cell body (item 2, Fig. 2*a*) is machined from a single block of Teflon®, and is the centrepiece upon which all of the other components are mounted. It features a set of ports

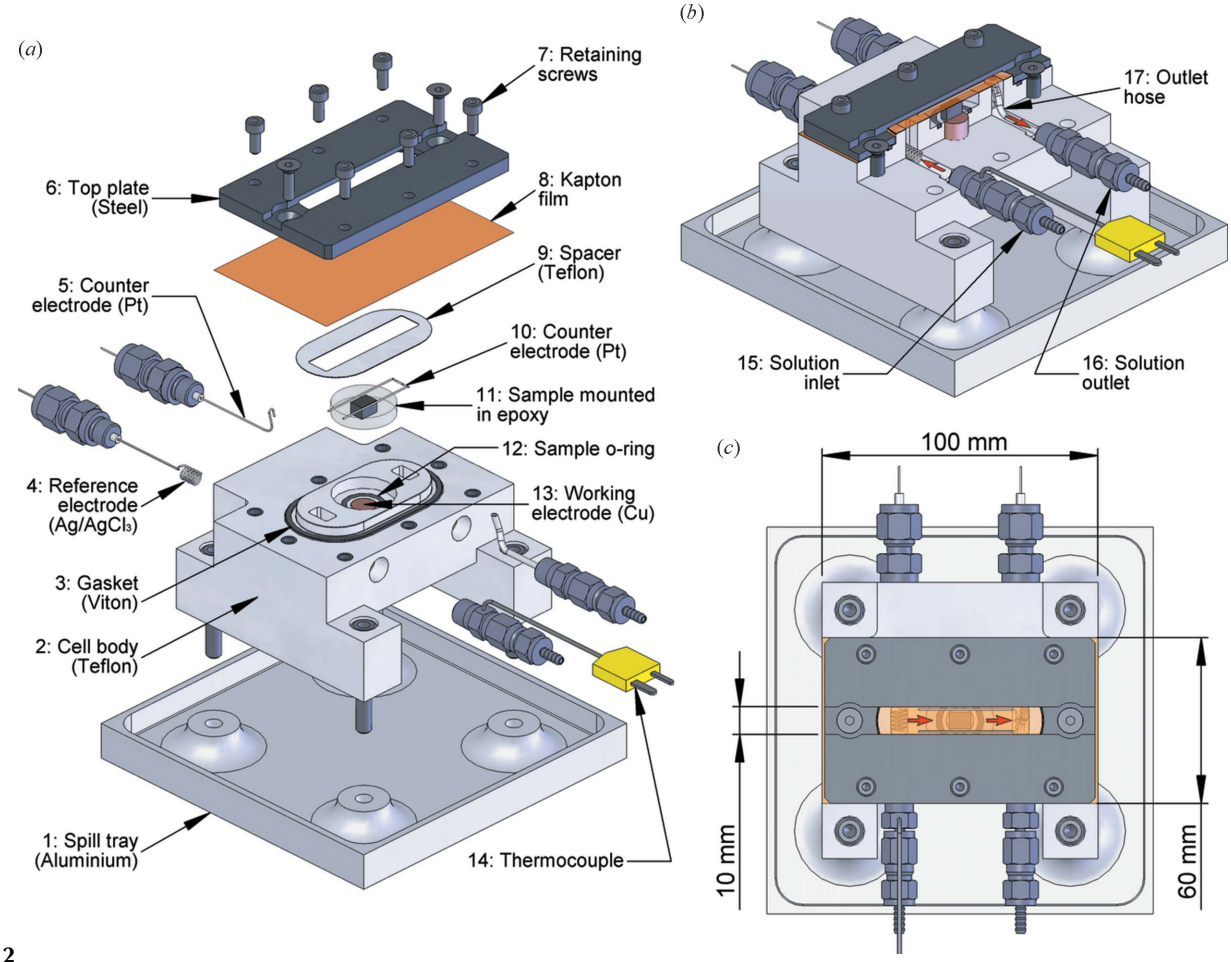

Figure 2
Schematic of the electrochemical flow cell (EFC). Part (*a*) shows an exploded view of the EFC, with the main components itemized (items 1 to 14). Part (*b*) shows a partial section view of the assembled EFC, highlighting the path taken by the flowing electrolyte solution (red arrows) through the inlet and outlet fittings (items 15 to 17). Part (*c*) shows a top view of the assembled EFC with some key dimensions.

and channels that enable a thin stream of solution to flow over a sample, positioned in the cylindrical cavity (25 mm diameter, 5 mm deep) located on the top surface, while also allowing the appropriate electrical connections to be made. In this cell, the reference (item 4, Fig. 2*a*) and counter (item 5, Fig. 2*a*) electrodes are $Ag/AgCl_3$ and Pt wire, respectively. These wires are sheathed in Teflon® tubing (sealed with epoxy) before being inserted into the cell body *via* stainless steel Swagelok tube fittings. The working electrode (item 13, Fig. 2*a*) is made from a threaded Cu rod that passes through the bottom of the cell body. The height of this rod can be adjusted, and is initially set to its lowest position to allow the sample to be inserted.

The electrolyte solution is fed into the cell through a stainless steel Swagelok tube fitting (item 15, Fig. 2*b*) located directly opposite the reference electrode (item 4). A T-type thermocouple (item 14, Fig. 2*a*) is inserted through a hole drilled in the side of this inlet fitting (sealed with epoxy), such that the tip of the thermocouple contacts the flowing electrolyte. The solution is drained out of the cell through another Swagelok tube fitting (item 16, Fig. 2*b*) located directly opposite the counter electrode (item 5). In order to ensure that any bubbles generated by the electrochemical process are also drained from the cell, a flexible Teflon® tube (item 17, Fig. 2*b*) is connected to the outlet tube fitting (also sealed with epoxy), and positioned such that solution effectively drains from the highest point in the cell. Although the cell is typically inclined during the *in situ* S-XRD measurements in such a way that the outlet fitting is higher than the inlet fitting, this arrangement with the outlet tube allows bubbles to be efficiently removed from the cell even when it is operated on a level surface.

The sample material, in this case pure (99.99%) Pb, is cut to approximate dimensions (L × W × D) of 7 mm × 6 mm × 6 mm, then carefully centred in a 25 mm-diameter mould and mounted in epoxy resin. Once cured, the surface of the mounted sample is ground and polished until the thickness (D) of the disk is in the 4.9–5.0 mm range. The sample (item 11, Fig. 2*a*) is then placed on top of a Viton® fluoroelastomer O-ring (item 12, Fig. 2*a*) in the cavity of the cell body. A small amount of vacuum grease is added to the bottom edge of the sample disk, in order to improve the seal between the sides of the disk and the cavity. The counter electrode is extended over the top of the sample using a second Pt wire (item 10, Fig. 2*a*), bent into a U-shape, that hooks onto the first Pt wire (item 5, Fig. 2*a*). A 200 µm-thick Teflon® spacer (item 9, Fig. 2*a*) is placed over the sample and the raised face of the cell body, and then a 25 µm-thick Kapton® film (item 8, Fig. 2*a*) is placed over the spacer. Kapton® was selected as the X-ray window material because of the lack of dominant peaks in its diffraction pattern, and because it withstood attack from the acid electrolyte.

A stainless steel top-plate (item 6) is then pushed down over the film and fixed to the cell body using stainless steel screws (item 7). The top plate is designed such that, once the cell is assembled, the top surface of the channel sits below the height of the sample surface, enabling low incident beam-to-sample angles. Tightening of the screws results in tensioning of the Kapton® film and, together with the Teflon® spacer (item 9), creates a defined flow region over the sample. Spacers of different thicknesses (within a certain range) may be used to alter the thickness of the electrolyte solution flowing over the sample depending on the X-ray attenuation in the electrolyte. Tightening the screws also pushes the lower surface of the top-plate onto the large Viton® gasket (item 3, Fig. 2*a*), sealing the cell and preventing leaks of corrosive solution. In addition, tightening the screws also pushes the sample onto the O-ring (item 12), sealing the Cu working electrode connector (item 13) from the electrolyte.

The exact positioning of the second Pt wire (item 10, Fig. 2*a*) is carried out in conjunction with pushing the stainless steel top plate down onto the Kapton® film. Care must be taken so that the Pt wire does not touch the working electrode (Pb anode) at any stage during the electrochemical test. This configuration, with the two halves of the Pt wire running parallel to the flow direction, allows any bubbles formed on the counter electrode to be quickly swept away by the electrolyte. This feature improved the electrochemical performance of the cell significantly, relative to an initial counter electrode design similar to the reference electrode (item 4, Fig. 2*a*). At the final stage of cell assembly, the Cu working electrode connector (item 13, Fig. 2*a*) is raised vertically so as to achieve good electrical contact with the underside of the working electrode (Pb anode). An additional feature of the EFC is a spill tray (item 1, Fig. 2*a*), designed to attach to the *XYZ* stage of the beamline and protect the stage in the event of any electrolyte leaks or spills.

2.2. Cell implementation during *in situ* experimentation

In situ S-XRD experiments were performed on the powder diffraction beamline at the Australian Synchrotron, equipped with a Mythen microstrip detector (Schmitt *et al.*, 2003) spanning 80° 2θ [A in Fig. 3(*a*)]. 500 ml of the 1.6 *M* H_2SO_4 electrolyte solution was heated to 323 K and stirred within a covered 3 L stainless-steel reservoir [B in Fig. 3(*a*)] using a digital hotplate and a magnetic stirrer. The EFC (D) was connected to the *XYZ* stage (E) of the diffractometer. A PVC spill tray was bolted to the top of the end-station table (F). The electrolyte was re-circulated from the reservoir, through the EFC and back to the reservoir at a rate of 40 ml min^{-1} through Viton® tubing using a peristaltic pump (C). The temperature of the electrolyte entering the EFC was recorded to be 318 K.

S-XRD data were collected throughout the six electrochemical cycles (see §2.3) with individual data sets collected for 1 min at each of two detector positions P1 and P2 (the Mythen detector contains 0.2° gaps every 5° 2θ; data were collected at two detector positions 0.5° apart in order to cover the entire 2θ range). The data were collected in asymmetric diffraction geometry with an incident beam-to-sample angle (defined hereafter as ω) of 8°, over the range $10° \leq 2\theta \leq 90°$. The vertical and horizontal slit widths were 0.2 and 5.0 mm, respectively. The X-ray wavelength was 0.9998 Å and was

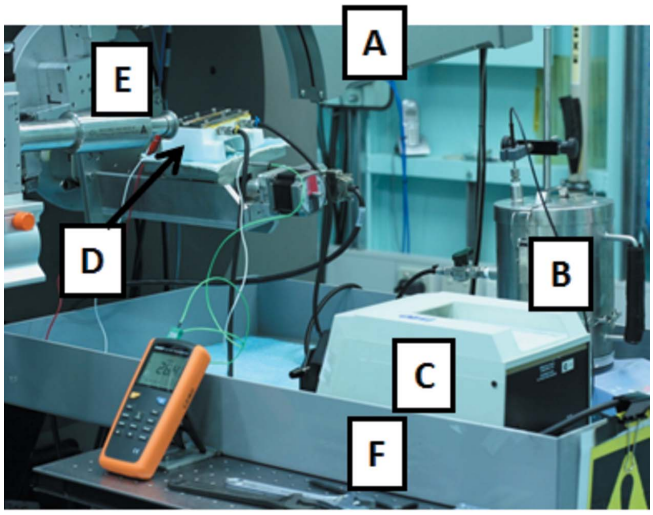

(*a*)

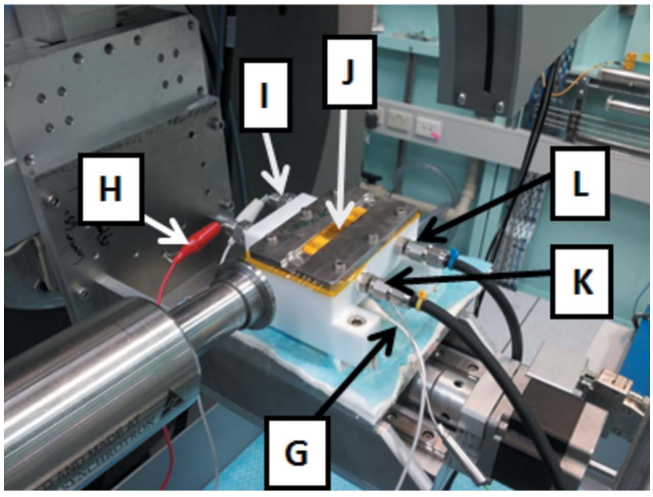

(*b*)

Figure 3
(*a*) Experimental setup for the *in situ* X-ray diffraction studies on the powder diffraction beamline at the Australian Synchrotron, and (*b*) the electrochemical flow cell. (A) Mythen detector; (B) electrolyte reservoir; (C) peristaltic pump; (D) flow cell; (E) *XYZ* stage; (F) spill tray; (G) working electrode lead; (H) reference electrode lead; (I) counter electrode lead; (J) Pb substrate; (K) electrolyte inlet; (L) electrolyte outlet.

calibrated using LaB_6 (NIST 660b line position standard) contained in a 0.3 mm-inner-diameter glass capillary.

2.3. Electrochemical conditions

The working electrode (Pb anode) was exposed to a galvanostatic (GALV) current by means of a BioLogic SP-150 potentiostat in conjunction with EC-Lab software. The applied current was equal to that used in some tank-houses, such that the current density was 300 A m^{-2}. After 40 min of applied GALV current, the OCP was recorded for a 30 min period, during which no current or voltage was applied to the system. This experiment was designed to examine the performance of the Pb anode during a tank-house power failure or when the power is switched off. The GALV segment, followed by the OCP segment, which made up one cycle, was repeated a further five times to record the evolution of the electrochemical performance of the Pb anode. It should be noted that the Ag/AgCl reference electrode has a potential difference of +0.199 V *versus* the normal hydrogen electrode (NHE). The potentiostat was connected to the cell *via* leads to the working electrode [G in Fig. 3(*b*)], the Ag/AgCl reference electrode (H) and the Pt counter electrode (I).

2.4. Data analysis

For the purposes of visualization of the decomposition and formation of phases as the electrochemical experiment progressed, individual P1 and P2 data sets were merged using *CONVAS2* (Rowles, 2010) to remove the detector gaps. The merged data sets were stacked to produce a plot of accumulated data with elapsed time plotted *versus* 2θ, viewed down the intensity axis. The merged data sets were also used for Rietveld refinement-based quantitative phase analysis (QPA) implemented in the launch mode of *TOPAS* (Bruker, 2009). Phase concentration values are relative crystalline wt% values calculated *via* the Hill & Howard (1987) algorithm. The crystal structure information provided by Straumanis (1949), D'Antonio & Santoro (1980) and Goodwin & Whetstone (1947) were used for Pb, β-PbO_2 and $PbSO_4$, respectively. A correction to account for sample displacement error in the asymmetric diffraction geometry (Madsen *et al.*, 2010) was incorporated into the refinement model. Also incorporated was an intensity correction [equation (3)], I_{cor}, to account for the asymmetric diffraction geometry and also the absorption of the diffracted X-rays in H_2SO_4 (after Egami & Billinge, 2003):

$$I_{cor} = I\left[2\Big/\left(1+\frac{\sin\omega}{\sin\beta}\right)\right]\exp\left(-\frac{\mu s}{\sin\beta}\right), \qquad (3)$$

where ω is 8° and β is the angle of the diffracted beam to the detector (reflection-dependent and equal to $2\theta - \omega$), and μ and s are the linear X-ray absorption coefficient and thickness of the electrolyte, respectively.

A relatively simple anisotropic crystallite size broadening function was selected to account for the observed peak profiles for the β-PbO_2 phase, to improve the quality of fit of the profile calculated using the conventional crystallite size and micro-strain models. This function is an adaptation of the March–Dollase (Dollase, 1986) preferred orientation model proposed by Coelho (2009), whereby the width (instead of intensity) of a given reflection is scaled based on its angular alignment with a particular crystallographic direction, introducing only one additional refinable parameter. This scaling factor was applied to the Lorentzian crystallite size and micro-strain functions as shown in equations (4) and (5), respectively,

$$\mathrm{FWHM}_{\mathrm{Lor}}(hkl) = \left[\frac{\lambda}{C\cos(\theta)}\right] \times \left[r^2\cos^2(\alpha_{hkl}) + r^{-1}\sin^2(\alpha_{hkl})\right], \qquad (4)$$

$$\mathrm{FWHM}_{\mathrm{Lor}}(hkl) = [m\tan(\theta)] \times \left[r^2\cos^2(\alpha_{hkl}) + r^{-1}\sin^2(\alpha_{hkl})\right]. \qquad (5)$$

Here, λ is the wavelength of the X-ray beam, C is the crystallite size parameter, m is the microstrain parameter, θ is the diffraction angle, r is the March parameter and α_{hkl} is the angle between the individual reflection (hkl) and a defined axis direction (HKL, in this case the 110 direction).

For the purposes of calculation of the thickness (t) of the $PbO_2/PbSO_4$ surface layer as a function of time, the decay in intensity (I/I_0) of the (111) Pb reflection at 20.2° 2θ was implemented in equation (6) (Cullity, 1978),

$$\frac{I}{I_0} = \exp\left[-\mu t\left(\frac{1}{\sin\omega} + \frac{1}{\sin\beta}\right)\right], \qquad (6)$$

where μ in this case is the X-ray linear absorption coefficient of the $PbO_2/PbSO_4$ surface layer. The relative concentrations of PbO_2 and $PbSO_4$ returned from the QPA were used to calculate the value of μ at each datapoint. This approach assumes 100% packing density of the surface layers, and is treated as a semi-quantitative approach only without accurate knowledge of the packing density as a function of time.

As a final comment on the experimental procedures, the incident beam angle (ω) was selected after consideration of Fig. 4, which shows the calculated effect, as a function of 2θ, of the experiment geometry on the absolute diffracted intensities for different ω values, assuming an electrolyte layer thickness of 200 µm. This geometry intensity factor (GIF) was calculated using equation (7), which is similar to equation (3) but also takes into account absorption of the *incident* X-ray beam in the H_2SO_4 electrolyte (Egami & Billinge, 2003). Based on these calculations, 8° was selected in order to provide a compromise between low- and high-angle intensities, whilst also ensuring the intensities of the major reflections for the possible surface phases [*i.e.* the (110), (211) and (111) reflections for β-PbO_2, $PbSO_4$ and α-PbO_2, respectively] were close to being maximized.

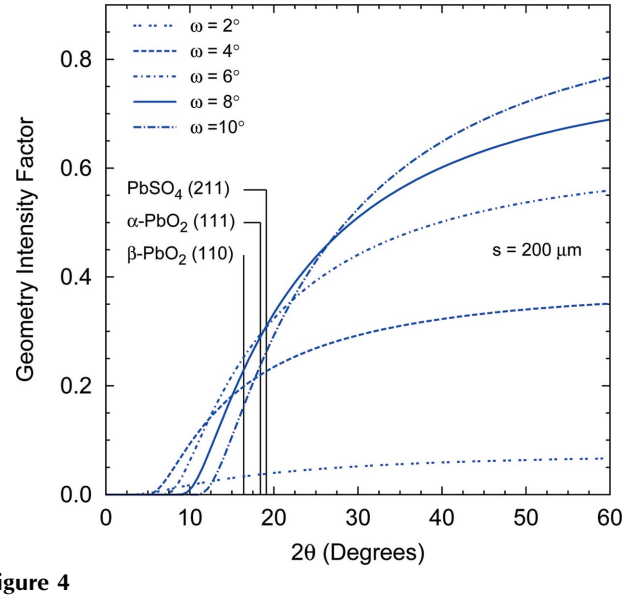

Figure 4
Plots, generated using equation (7), of the geometry intensity factor (GIF) as a function of 2θ for ω values of 2, 4, 6, 8 and 10°, and for an electrolyte thickness of 200 µm.

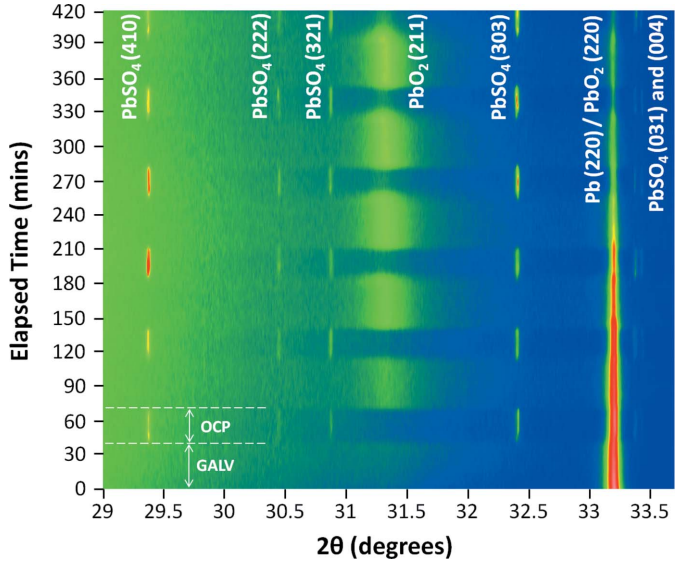

Figure 5
A plot of accumulated diffraction data collected for the Pb anode during electrochemical cycling, where GALV = galvanostatic and OCP = power interruption regimes.

$$\mathrm{GIF} = \left[2\Big/\left(1 + \frac{\sin\omega}{\sin\beta}\right)\right]\exp\left(-\frac{\mu s}{\sin\omega} - \frac{\mu s}{\sin\beta}\right). \qquad (7)$$

3. Results and discussion

3.1. Phase behaviour

Fig. 5 shows the plot of accumulated *in situ* S-XRD data. The first of the six GALV and OCP segments are labelled. During the GALV segments, the tetragonal β-PbO_2 [International Centre for Diffraction Data (ICDD) database number 41-1492] formed, while the orthorhombic form of $PbSO_4$ (ICDD 36-1461) formed during the OCP segments. Other than those from the Pb substrate (ICDD 4-0686), reflections from no other phases were observed during the experiment. A shift of the broad PbO_2 reflections to lower 2θ during conversion of this phase to $PbSO_4$ was observed; in contrast, there was no systematic shift of the $PbSO_4$ reflections observed over the duration of the experiment. The shift in the PbO_2 reflections is attributed to substitution of larger Pb^{2+} (ionic radius = 1.33 Å) (Shannon, 1976) cations for Pb^{4+} (0.915 Å) in the β-PbO_2 structure during conversion to $PbSO_4$, forming a non-stoichiometric phase (Butler & Copp, 1956). None of the previous *in situ* studies performed in this context (Herron *et al.*, 1992*b*; Nauer, 1996; Angerer *et al.*, 2009) described such a peak shift, which is a demonstration of the benefit of the continuous data collection which this flow cell allows.

3.2. Electrochemical behaviour

The electrochemical response of the Pb anode to the applied current in the sulfuric acid electrolyte is presented in Fig. 6. The results of the laboratory-based electrochemical

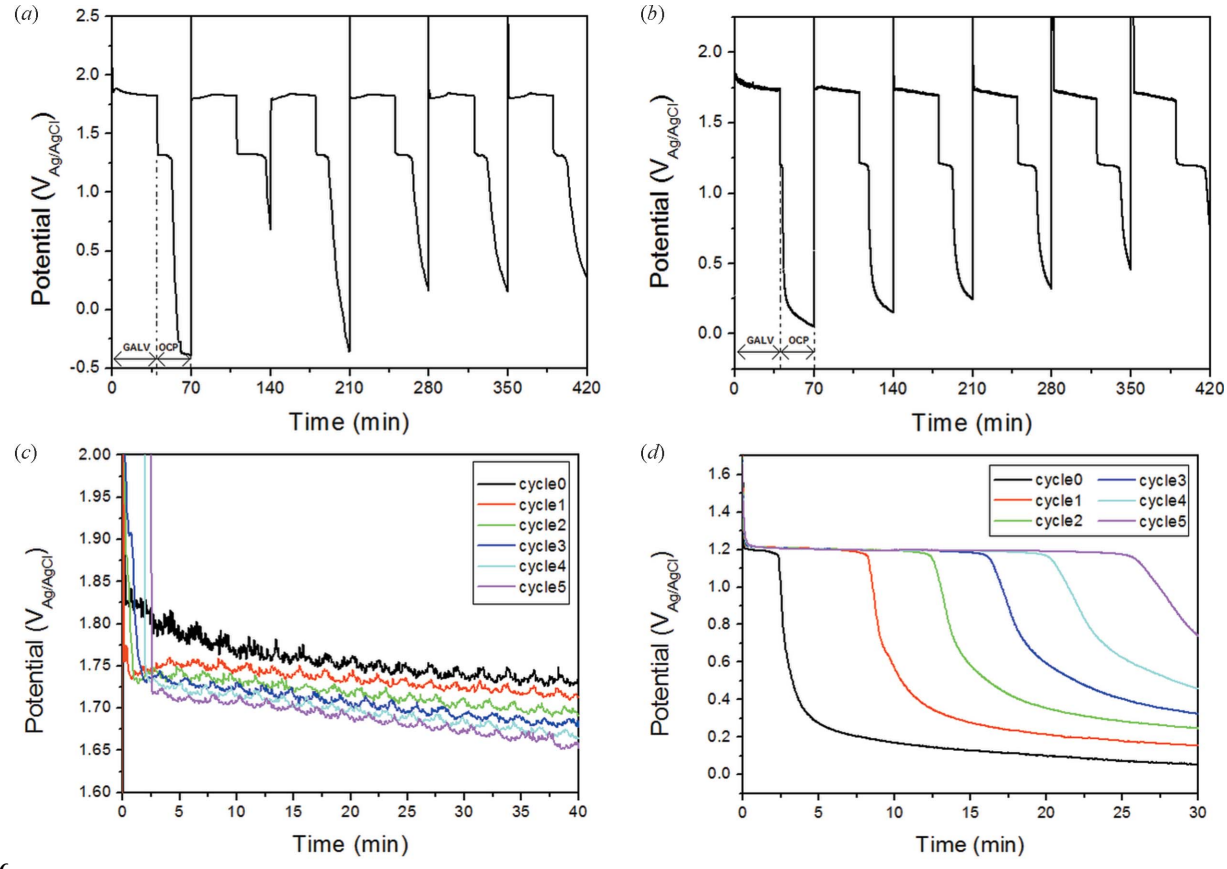

Figure 6
Potential *versus* time plots for the Pb anode in (*a*) standard *ex situ* BioLogic flat cell in conventional laboratory and (*b*) the EFC used for the *in situ* synchrotron experiments. While the scans are relatively comparable, there will be differences due to the electrolyte not being pumped through the system in (*a*) and it being pumped through the EFC in (*b*). Differences in the cell and counter electrode geometry could also be factors. The plots in (*c*) and (*d*) are simply galvanostatic and power interruption/OCP segments graphed together for comparative purposes. The pulses that are evident in (*c*) are due to a pump that was pushing the heated electrolyte through the system.

testing program which utilized standard electrochemical apparatus and the results from the *in situ* EFC experiment are shown in Figs. 6(*a*) and 6(*b*), respectively. The electrochemical performance of the Pb anode under regular laboratory conditions is comparable with that of the *in situ* experiments. The very minor differences in potential of only a few mV are attributed to the adjustment to present the same reference scale as the laboratory experiment using a saturated calomel electrode while the *in situ* experiment used an Ag/AgCl reference electrode. However, the differences are not noteworthy. The geometry of the two cells was also quite different, with the working electrode being vertical on one wall of the flat cell with the stationary electrolyte adjacent to it for the laboratory-based experiment, while for the *in situ* experiment the working electrode lay horizontal, in the centre of the cell, with the electrolyte flowing over it as it was pumped through the system. In Figs. 6(*c*) and 6(*d*) the GALV and OCP segments are plotted separately, further highlighting the evolving behaviour of the system with each cycle.

The OCP decay curves, as shown in Fig. 6(*c*), are indicative of the dissolution of the anodic (PbO_2) layer, otherwise referred to as 'self-decay' (Ruetschi, 1973). As the OCP potential of Pb has previously been measured to be approximately $-0.556\ V_{Ag/AgCl}$ it is evident that the system in this present study did not achieve its assumed OCP within the given time frame, hence there will not have been complete dissolution of the surface layer. The first five minutes in Fig. 6(*c*) are quite interesting and these are comparable with the moment when the power is cut to an electrowinning cell, or the moment when a battery is switched from charging to discharging mode. It appears that, as the cycles progress, it takes longer for the potential to start to stabilize, but once it does start to do so it is at a lower potential than its predecessor. This may be attributed to the increased growth and stabilization of the PbO_2 phase, which correlates with the data presented in Fig. 8(*a*) (see §3.3 for discussion). In Fig. 6(*c*) the decrease in the measured potential for each cycle, in comparison with the previous one, is significant, with each cycle measuring an average of 15 mV less than the cycle prior to it. Each cycle stabilized at almost the same rate, but the factor which controlled the measured potential at 40 min was the starting behaviour at 0–5 min. Fig. 6(*d*) shows the response of the Pb anode for each OCP segment. There are a number of interesting responses here to note. Each OCP segment had the same initial response, in that the potential decreased to $\sim 1.2\ V_{Ag/AgCl}$. The system held this potential for an increasing length of time with each cycle, *i.e.* 2.5, 8, 12.5, 16, 20 and 25 min for cycles 0–5, respectively. This plateau has been reported

previously (Ruetschi, 1973) and the potential at which it occurred in this system is in agreement with that of Ruetschi. The rate at which the potential further declined slowed with each additional cycle and the overall drop in the potential also reduced. The minimum potential reached during the OCP segment of cycle 0 was 0.05 V while the minimum potential during the OCP segment of cycle 5 was 0.75 V.

3.3. Quantitative phase analysis and thickness evolution

Fig. 7(*a*) shows the Rietveld fit to a dataset collected during the OCP segment of the fifth cycle (after 320 min); Fig. 7(*b*) shows an overlay of (i) the dataset collected at the beginning of the first GALV segment after electrolyte flow had commenced, and (ii) the dataset collected for the substrate and Kapton® film before the flow of electrolyte had commenced, and demonstrates that the high background in Fig. 7(*a*) is due predominantly to scatter from the electrolyte.

Fig. 8(*a*) shows the results of the Rietveld-based QPA. The maximum errors in Pb, β-PbO_2 and $PbSO_4$ concentrations from the Rietveld refinements, indicative of the error in fit between the experimental and calculated intensities, were 0.9, 0.8 and 0.7 wt%, respectively. PbO_2 formed immediately on the substrate, and continued to grow during the GALV segment of the first cycle, as indicated by the increase in crystalline phase concentration from 20 wt% at t = 0 min to 37 wt% at the end of the segment (t = 38 min). The steady reduction in the potential throughout the GALV segment in the first cycle, and indeed in each subsequent GALV segment [Fig. 6(*b*), and shown again in Fig. 8(*b*) for ease of comparison with Fig. 8(*a*)] was attributed to growth and stabilization of the PbO_2 layer. The concentration of PbO_2 also increased as the number of cycles increased; PbO_2 represented ~43 wt% at the start of the GALV segment of the second cycle (t = 74 min), compared with 19 wt% at the end of the GALV segment of the first cycle, for example, and the progressive decrease in the measured potential for each cycle is attributed to this. It is apparent in Fig. 8(*a*) that the PbO_2 to $PbSO_4$ transformation at the GALV to OCP transition in the first cycle is rapid, and as the number of cycles increased this transition time also increased. The increasing resilience of

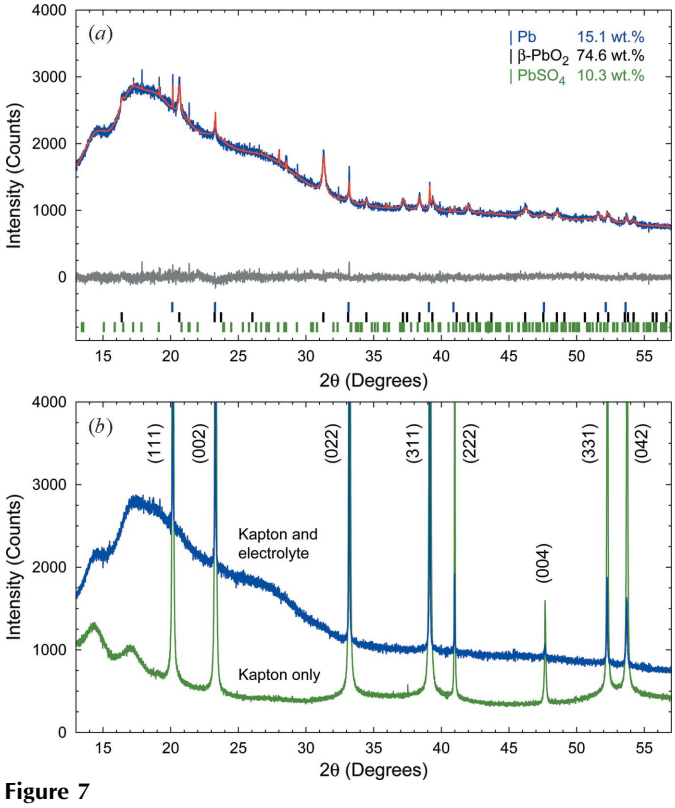

Figure 7
(*a*) Rietveld refinement output of a dataset collected during the early stages of the OCP segment of the fifth cycle (t = 320 min, R_{wp} = 2.56). The experimental data are shown as a blue solid line, the calculated pattern the red solid line, and the difference pattern the grey solid line below. The tick marks below the difference curve are the Bragg reflection markers for Pb (upper), β-PbO_2 (middle) and $PbSO_4$ (lower). (*b*) Overlay of datasets collected at the beginning of the first GALV segment (upper), and for the substrate and Kapton® film before the flow of electrolyte commenced (lower). The Pb reflections are labelled with their Miller indices.

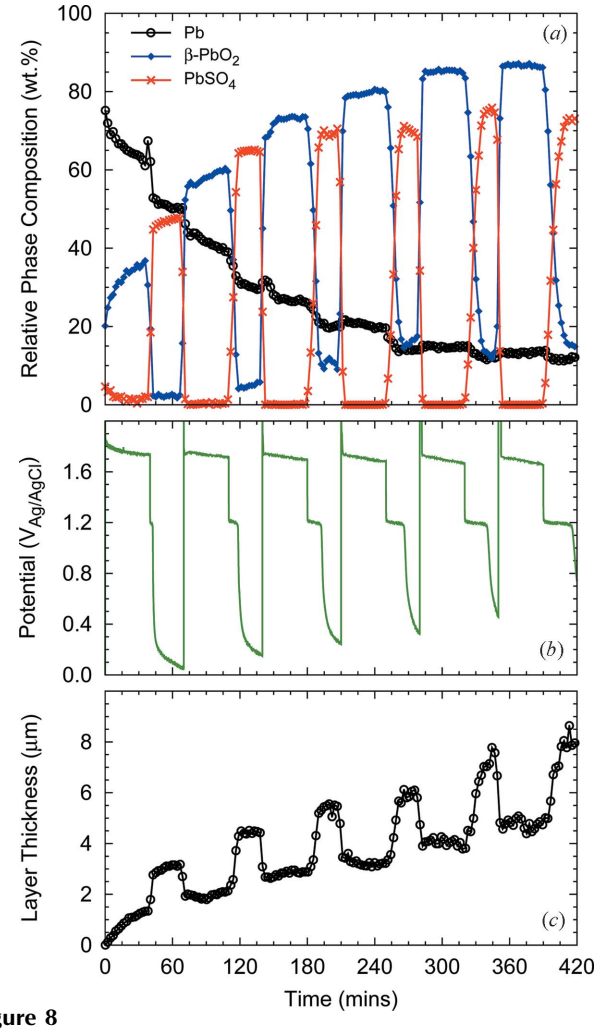

Figure 8
(*a*) Results of Rietveld refinement-based quantitative phase analysis, showing the evolution in relative concentration of the Pb substrate and the PbO_2 and $PbSO_4$ surface layers during the electrochemical test. (*b*) Potential *versus* time plot. (*c*) Estimated PbO_2/$PbSO_4$ surface layer thickness as a function of time.

the PbO_2 layer to the power interruption is the cause of the progressively longer plateau at 1.2 $V_{Ag/AgCl}$ in Fig. 6(*c*). Finally, whilst at each of the OCP to GALV transitions the $PbSO_4$ transforms completely, the dissolution of PbO_2 at the GALV to OCP transitions is incomplete and the amount of residual PbO_2 increases and reaches 17 wt% in the final cycle. The decrease in the difference in the potential at the start and finish of each OCP segment shown in Fig. 6(*c*) is attributed to retained PbO_2 and this is further proven by Fig. 8(*a*). This graph clearly shows that, with increasing time and increased cycling, the PbO_2 layer dominates. This suggests that the $PbO_2 \leftrightarrow PbSO_4$ transformation does not have sufficient time to proceed to completion. Not only that, the activation energy for the $PbSO_4 \rightarrow PbO_2$ transformation may reduce with time.

An additional comment in relation to the data in Fig. 8(*a*) is that an insight is provided into one of the major questions posed in section 1, as to whether or not the surface becomes a homogeneous layer or a multiphase system? This has now been detailed for each of the GALV and OCP regimes in each of the cycles.

Fig. 8(*c*) shows the results of the $PbO_2/PbSO_4$ layer thickness calculation using the relationship shown in equation (6). Since PbO_2 was present on the surface of the anode at t = 0 min [the concentration of PbO_2 in Fig. 7(*a*) is 20 wt%], the I_0 value used here in equation (6) is not the true I_0 value for a layer-free surface, which adds to the semi-quantitative nature of this approach. Nevertheless, what is striking about this plot is that it suggests a consistent layer thickness decrease of $\sim$50% upon conversion of $PbSO_4$ to PbO_2. This is in accordance with the volume decrease reported in the literature (Burbank, 1966; Deutscher *et al.*, 1985; Pavlov *et al.*, 1990; Pavlov, 2011). Again, this demonstrates the effectiveness of the flow cell and associated experimentation in characterizing the surface layer evolution on the Pb substrate.

4. Conclusion

This paper has described the design and implementation of a new electrochemical flow cell which enables the evolution of surface layers to be characterized under genuine operating conditions of an electrochemical cell. It has been used here to characterize the evolution of surface layers formed on a Pb anode under electrochemical conditions which simulate both normal operation (GALV) and power interruption (OCP) conditions in industrial Cu electrowinning. The flow cell, in conjunction with the S-XRD and the electrochemical programming, were successful in quantitatively assessing, in real time, how the surface layer evolves. This system and experimental design can have a valuable impact on the electrowinning industry, in investigating how the preferable PbO_2 phase can be maintained and what might actually be the minimum (trickle) current required to maintain the layer on the surface, thus preventing reversion to $PbSO_4$.

With regards to the PbO_2, there was no trace of the α polymorph. This is in agreement with Ivanov *et al.* (2000) who proposed that this polymorph of the oxide preferentially forms in alkaline media. This study herein has shown that the surface layers can alter from being a single-phase layer of β-PbO_2 during galvanostatic conditions to a multi-phase ($PbSO_4/\beta$-PbO_2) system during power interruption. With increased cycling the system actually retains more of the β-PbO_2 and shows less propensity to transform to $PbSO_4$. This is a favourable realisation as the oxide layer (as opposed to the sulfate layer) has more favourable properties. However the thickness of the surface layer was seen to increase with increased cycling. This is an undesirable development as ideally the surface layer needs to be as thin, dense and compact as possible in an effort to maintain good contact and adhesion to the underlying substrate. There is significant scope for more detailed electrochemical analysis using impendence spectroscopy or cyclic resistometry (Deutscher *et al.*, 1985) of the surface layer in future *in situ* experiments.

The design and successful performance of this experiment, with application in the electrowinning industry in mind, leads the way for even more *in situ* XRD and electrochemical analysis of the system, its complexities and relevant anode alloy development.

This research was undertaken on the powder diffraction beamline at the Australian Synchrotron, Victoria, Australia, under beam time award AS141/M7391. The authors wish to thank Richard Ciba, Greg Blease and Chris Kohle (CSIRO Clayton Engineering Facility) for construction of the flow cell, Mark Gibson (CSIRO Manufacturing Flagship) and Ian Madsen (CSIRO Mineral Resources Flagship) for helpful discussions and Jean-Pierre Veder and Mikko Vepsalainen (CSIRO Mineral Resources Flagship) for their assistance with the reference electrode preparation.

References

Angerer, P., Mann, R., Gavrilovic, A. & Nauer, G. E. (2009). *Mater. Chem. Phys.* **114**, 983–989.
Bagshaw, N. E., Clarke, R. L. & Halliwell, B. (1966). *J. Appl. Chem.* **16**, 180–184.
Barlow, N., Brennan, C., Doyle, S. E., Greaves, G. N., Miller, M., Nahle, A. H., Roberts, K. J., Robinson, J., Sherwood, J. N. & Walsh, F. C. (1989). *Rev. Sci. Instrum.* **60**, 2386–2389.
Bruker (2009). *TOPAS* Version 4.2, Bruker AXS Inc., Madison, WI, USA.
Burbank, J. (1966). *J. Electrochem. Soc.* **113**, 10–14.
Burbank, J. (1971). *J. Electrochem. Soc.* **118**, 525–529.
Butler, G. & Copp, J. L. (1956). *J. Chem. Soc.* p. 725.
Caballero, A., Cruz, M., Hernán, L., Morales, J. & Sánchez, L. (2004). *J. Power Sources*, **125**, 246–255.
Camurri, C. P., López, M. J., Pagliero, A. N. & Vergara, F. G. (2001). *Mater. Charact.* **47**, 105–109.
Clancy, M., Bettles, C. J., Stuart, A. & Birbilis, N. (2013). *Hydrometallurgy*, **131**–*132*, 144–157.
Coelho (2009). *Topas Academic Technical Reference*, Version 4.1, Coelho Software, http://www.topas-academic.net.
Cullity, B. D. (1978). *Elements of X-ray Diffraction*, 2nd ed., pp. 132–135. Reading: Addison-Wesley.
D'Antonio, P. & Santoro, A. (1980). *Acta Cryst.* B**36**, 2394–2397.
De Marco, R., Pejcic, B., Prince, K. & van Riessen, A. (2003). *Analyst*, **128**, 742–749.
Deutscher, R. L., Fletcher, S. & Hamilton, J. A. (1985). *Electrochim. Acta*, **31**, 585–589.
Dollase, W. A. (1986). *J. Appl. Cryst.* **19**, 267–272.

Egami, T. & Billinge, S. J. L. (2003). *Underneath the Bragg Peaks: Structural Analysis of Complex Materials*, pp. 210–218. Oxford: Elsevier.
Fletcher, S. & Matthews, D. B. (1981). *J. Electroanal. Chem. Interfacial Electrochem.* **126**, 131–144.
Goodwin, T. H. & Whetstone, J. (1947). *J. Chem. Soc.* pp. 1455–1461.
Herron, M. E., Doyle, S. E., Roberts, K. J., Robinson, J. & Walsh, F. C. (1992*a*). *Rev. Sci. Instrum.* **63**, 950–955.
Herron, M. E., Roberts, K. J., Doyle, S. E., Robinson, J. & Walsh, F. C. (1992*b*). *Phase Trans.* **39**, 135–144.
Hill, R. J. (1982). *Mater. Res. Bull.* **17**, 769–784.
Hill, R. J. & Howard, C. J. (1987). *J. Appl. Cryst.* **20**, 467–474.
Ingham, B., Ko, M., Kear, G., Kappen, P., Laycock, N., Kimpton, J. A. & Williams, D. E. (2010). *Corros. Sci.* **52**, 3052–3061.
Ivanov, I., Stefanov, Y., Noncheva, Z., Petrova, M., Dobrev, T., Mirkova, L., Vermeersch, R. & Demaerel, J. P. (2000). *Hydrometallurgy*, **57**, 125–139.
Ko, M., Laycock, N. J., Ingham, B. & Williams, D. E. (2012). *Corrosion*, **68**, 1085–1093.
Madsen, I. C., Grey, I. E. & Mills, S. J. (2010). *Mater. Sci. Forum*, **651**, 37–64.
Maksymiuk, K., Stroka, J. & Galus, Z. (2009). *Chemistry, Electrochemistry and Electrochemical Applications: Lead*, in *Encyclopedia of Electrochemical Power Sources*, edited by J. Garche, pp. 762–771. Amsterdam: Elsevier.
Marco, R. D. & Veder, J.-P. (2010). *TrAC Trends Anal. Chem.* **29**, 528–537.
Miyake, M., Minato, I., Morikawa, H. & Iwai, S. I. (1978). *Am. Mineral.* **63**, 506–510.
Monahov, B. & Pavlov, D. (1993). *J. Appl. Electrochem.* **23**, 1244–1250.
Nagy, Z., You, H. & Yonco, R. M. (1994). *Rev. Sci. Instrum.* **65**, 2199–2205.
Nauer, G. E. (1996). *Mater. Sci. Forum*, **228**–**231**, 387–392.
Nikoloski, A., Nicol, M. & Stuart, A. (2010). *Proceedings of Copper 2010*, 6–10 June 2010, Hamburg, Germany, pp. 1559–1568.
Pavlov, D. (2011). *Lead-Acid Batteries: Science and Technology.* Amsterdam: Elsevier.
Pavlov, D., Bashtavelova, E., Simonsson, D. & Ekdunge, P. (1990). *J. Power Sources*, **30**, 77–97.
Pavlov, D., Kirchev, A., Stoycheva, M. & Monahov, B. (2004). *J. Power Sources*, **137**, 288–308.
Pavlov, D. & Monahov, B. (1996). *J. Electrochem. Soc.* **143**, 3616–3629.
Rayment, T., Davenport, A. J., Dent, A. J., Tinnes, J. P., Wiltshire, R. J. K., Martin, C., Clark, G., Quinn, P. & Mosselmans, J. F. W. (2008). *Electrochem. Commun.* **10**, 855–858.
Robinson, K. M. & O'Grady, W. E. (1993). *Rev. Sci. Instrum.* **64**, 1061.
Rowles, M. R. (2010). *Powder Diffr.* **25**, 297–301.
Ruetschi, P. (1973). *J. Electrochem. Soc.* **120**, 331–336.
Scherb, G., Kazimirov, A. & Zegenhagen, J. (1998). *Rev. Sci. Instrum.* **69**, 512–516.
Schlesinger, M., King, M., Sole, K. & Davenport, W. (2011). *Extractive Metallurgy of Copper*, ch. 17. Amsterdam: Elsevier.
Schmitt, B., Brönnimann, C., Eikenberry, E. F., Gozzo, F., Hörmann, C., Horisberger, R. & Patterson, B. (2003). *Nucl. Instrum. Methods Phys. Res. A*, **501**, 267–272.
Shannon, R. D. (1976). *Acta Cryst.* A**32**, 751–767.
Straumanis, M. E. (1949). *J. Appl. Phys.* **20**, 726–734.
Taggart, J. E., Foord, E. E., Rosenzweig, A. & Hanson, T. (1988). *Can. Mineral.* **26**, 905–910.
Wallwork, K. S., Kennedy, B. J. & Wang, D. (2007). *AIP Conf. Proc.* **879**, 879–882.
Webster, N. A. S., Madsen, I. C., Loan, M. J., Scarlett, N. V. Y. & Wallwork, K. S. (2009). *Rev. Sci. Instrum.* **80**, 084102.
White, W. B., Dachille, F. & Roy, R. (1961). *J. Am. Ceram. Soc.* **44**, 170–174.
White, W. B. & Roy, R. (1964). *J. Am. Ceram. Soc.* **47**, 242–249.
Xia, S. J. & Zhou, W. F. (1995). *Electrochim. Acta*, **40**, 181–187.